ACS NANO
Cite This: ACS Nano 2018, 12, 9441−9450
www.acsnano.org

ARTICLE

High-Density Ultra-small Clusters and Single-Atom Fe Sites Embedded in Graphitic Carbon Nitride (g-C_3N_4) for Highly Efficient Catalytic Advanced Oxidation Processes

Sufeng An,[†,#] Guanghui Zhang,[‡,#] Tingwen Wang,[†] Wenna Zhang,[§] Keyan Li,[*,†] Chunshan Song,[†,∥] Jeffrey T. Miller,[‡] Shu Miao,[§] Junhu Wang,[§] and Xinwen Guo[*,†]

[†]State Key Laboratory of Fine Chemicals, PSU-DUT Joint Center for Energy Research, School of Chemical Engineering, Dalian University of Technology, Dalian 116024, PR China

[‡]Davidson School of Chemical Engineering, Purdue University, West Lafayette, Indiana 47907, United States

[§]Dalian Institute of Chemical Physics, Chinese Academy of Sciences, Dalian, 116023, PR China

[∥]EMS Energy Institute, PSU-DUT Joint Center for Energy Research and Department of Energy & Mineral Engineering, The Pennsylvania State University, University Park, Pennsylvania 16802, United States

Supporting Information

ABSTRACT: **Ultra-small metal clusters have attracted great attention owing to their superior catalytic performance and extensive application in heterogeneous catalysis. However, the synthesis of high-density metal clusters is very challenging due to their facile aggregation. Herein, one-step pyrolysis was used to synthesize ultra-small clusters and single-atom Fe sites embedded in graphitic carbon nitride with high density (iron loading up to 18.2 wt %), evidenced by high-angle annular dark field-scanning transmission electron microscopy, X-ray absorption spectroscopy, X-ray photoelectron spectroscopy, and ^{57}Fe Mössbauer spectroscopy. The catalysts exhibit enhanced activity and stability in degrading various organic samples in advanced oxidation processes. The drastically increased metal site density and stability provide useful insights into the design and synthesis of cluster catalysts for practical application in catalytic oxidation reactions.**

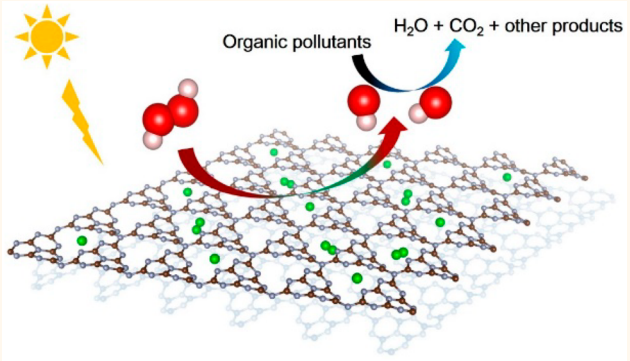

KEYWORDS: *ultra-small clusters, single atoms, FeN_x/g-C_3N_4, high-density, AOPs*

With society's needs for better quality of life and emphasis on sustainable development, environmental pollution has become one of the serious problems to be solved. In particular, water pollution is a major threat to human health, such that organic compounds (industrial dyes, pharmaceuticals, and pesticides, *etc.*) are main contaminants present in wastewater, rivers, and groundwater.[1,2] Various methods have been developed to deal with contaminated water, such as adsorption, flocculation, biological methods, and advanced oxidation processes (AOPs).[3−5] Among them, AOPs have gained considerable attention.[6−9] Heterogeneous Fenton-type Fe-based catalysts have been extensively used in AOPs, owing to their ease of separation, low cost, low toxicity, and environmental compatibility.[10,11] These Fe catalysts can activate H_2O_2 to generate hydroxyl radicals (HO·), one of the most powerful oxidants, which react with numerous organic compounds. However, most heterogeneous Fenton catalysts have large particles and wide particle size distribution due to the natural tendency for metal atoms to diffuse and agglomerate.[12,13] Various supports have been used to improve the catalyst dispersion and stability, including graphene, metal oxide, zeolite, *etc.*[14−17] However, most of these catalysts still suffer from low dispersion and stability, and thus, it is highly desirable to design efficient and stable Fe-based catalysts for AOPs.

Received: June 20, 2018
Accepted: September 5, 2018
Published: September 5, 2018

DOI: 10.1021/acsnano.8b04693
ACS Nano 2018, 12, 9441−9450

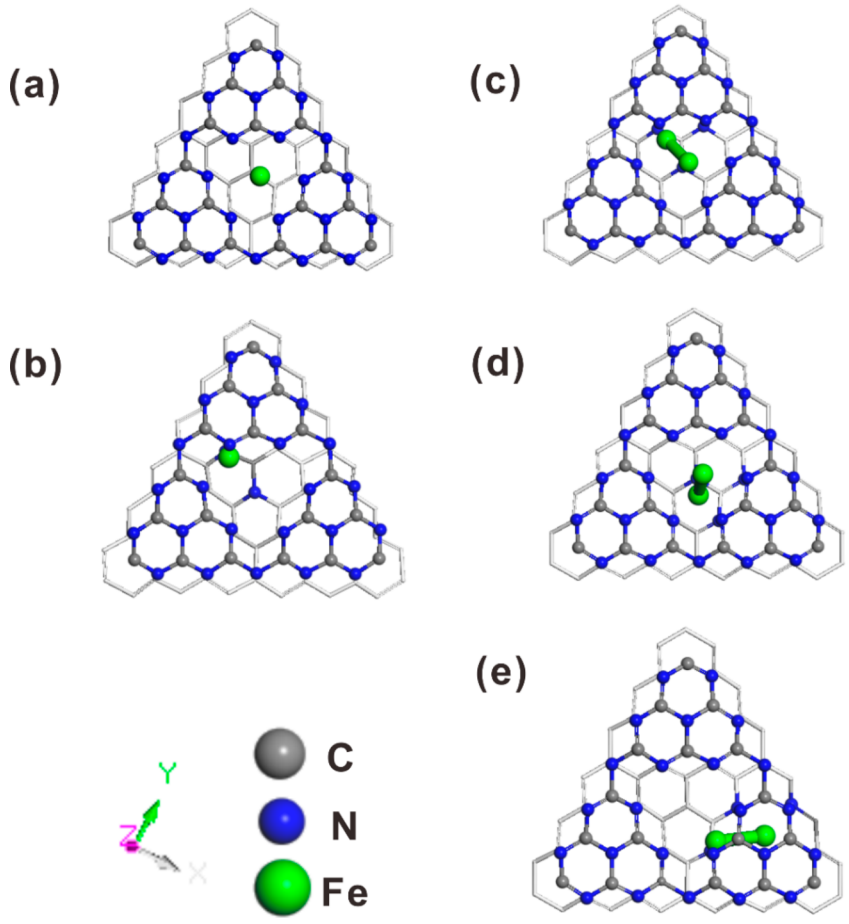

Figure 1. Optimized structures of various positions of single Fe atom and Fe cluster in g-C_3N_4. (a) Single Fe atom in the center of 6-fold cavity, (b) single Fe atom in interlayer, (c) Fe cluster in interlayer (Site1), (d) Fe cluster in interlayer (Site2), and (e) Fe cluster in interlayer (Site3).

The application of catalysts with ultra-small clusters and single-atom sites has attracted great interest because of their high atom-utilization efficiency.[18,19] Recently, preparation of such catalysts has been demonstrated in which the active sites are highly dispersed as sub-nanometer clusters, single atoms, or both, such as Pd−Ni$(OH)_2$@S-1, Pd@RCC3, Co−N−C, and Cu−N@C.[20−24] Single-atom Cu−N@C catalyst with high density of active sites has been achieved with a metal loading up to 8.5 wt %, suggesting the promising potential for practical application. Further increasing the density of the active sites requires a judicious selection of new support materials that can provide more anchoring sites and robust metal−support interaction to ensure high dispersion and stability. N-doped carbon has been used as a support to anchor ultra-small clusters and single-atom sites where the isolated metal species can bind to N atoms, providing stable catalysts.[25,26] However, the limited content of nitrogen dopants leads to limited anchoring sites. Taking advantage of the N coordination cavities, we anticipate that the low cost and environmentally friendly graphitic carbon nitride (g-C_3N_4) with high-density homogeneous "six-fold cavities" shall be a promising support for firmly trapping ultra-small clusters, single-atom Fe sites, or both.[27−29]

In this work, we designed a catalyst with ultra-small clusters and single-atom Fe sites embedded in g-C_3N_4 for catalytic oxidation reactions. The catalysts were prepared by a one-step pyrolysis of a mixture of Fe-imidazole coordination compound (Fe-ICC) and melamine (MA). High-density Fe sites with ultrahigh Fe loading up to 18.2 wt % were obtained with high dispersion, as evidenced by high-angle annular dark field-scanning transmission electron microscopy (HAADF-STEM), X-ray absorption spectroscopy (XAS), ^{57}Fe Mössbauer spectroscopy, and X-ray photoelectron spectroscopy (XPS). These catalysts exhibit excellent activity for degrading various model organic pollutants in AOPs, thus showing promising potential for practical application.

RESULTS AND DISCUSSION

g-C_3N_4 is emerging as a promising support to stabilize high-density ultra-small metal clusters and single-atom sites due to its homogeneous high-density N atoms and "six-fold cavities" for firmly trapping transition metals. Several recent studies have successfully dispersed single noble metal atoms on g-C_3N_4, and density functional theory (DFT) calculations suggested that Pd/Pt atoms can be stabilized at various positions of g-C_3N_4.[30,31] We propose g-C_3N_4 should also be able to stabilize high-density ultra-small clusters and single-atom Fe sites. This hypothesis was first verified by DFT calculations. We calculated the Fe binding energy at various adsorption sites in g-C_3N_4. The stable configurations for adsorption of a single Fe atom are shown in Figure 1a,b. Other initial adsorption configurations converged to these two sites, with strong preference for the Fe atom to move to the center of the 6-fold cavity. At the center of the 6-fold cavity, a single

DOI: 10.1021/acsnano.8b04693
ACS Nano 2018, 12, 9441−9450

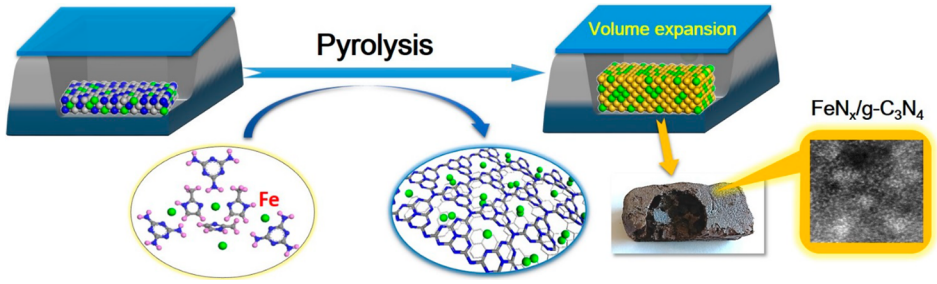

Figure 2. Pyrolytic synthesis of FeN_x/g-C_3N_4 catalysts.

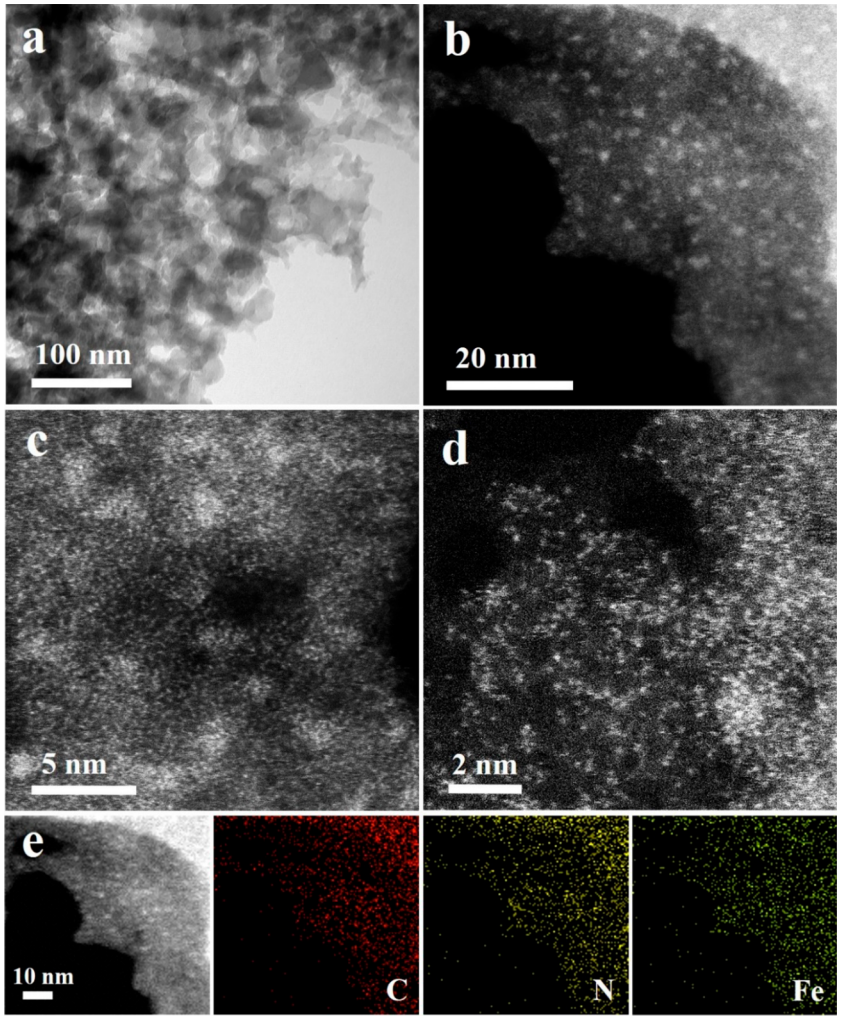

Figure 3. (a) TEM image; (b–d) HAADF-STEM images; and (e) the corresponding element mappings for the C, N, and Fe atoms of I-FeN_x/g-C_3N_4-5 catalyst.

Fe atom can be stable due to the relatively low binding energy of −2.77 eV (Figure 1a). The most stable adsorption site (Figure 1b), with a binding energy of −3.92 eV (Table S1), places the Fe atom between two layers of g-C_3N_4 interacting with N atoms above and below. The location of Fe_2 dimer was also examined as a model of ultra-small Fe clusters. All considered configurations optimized to place the Fe_2 dimer between layers (Figure 1c–e) with a binding energy of −2.50 to −2.83 eV. The Fe_2 dimer is only stable in the interlayer region. The considerably weaker binding (per Fe atom) of the Fe_2 dimers versus single Fe atoms (−3.92 eV) in the interlayer confirms a preference of Fe atoms to remain isolated versus dimerized. The calculation results support the feasibility of dispersing high-density cluster and single-atom Fe sites in g-C_3N_4 matrix.

As shown in Figure 2, the synthesis of I-FeN_x/g-C_3N_4-*X* (*X* represents the mass ratio of MA over Fe-ICC) was carried out *via* a one-step pyrolysis of Fe precursors and MA. The presynthesized Fe-ICC and MA were ground and pyrolyzed at 600 °C in a N_2 atmosphere. For comparison, M-FeN_x/g-C_3N_4-*X* and S-FeN_x/g-C_3N_4-*X* were also synthesized by pyrolysis of MA/MIL-53(Fe) (an Fe-based metal organic framework with 1, 4-benzenedicarboxylate ligands) and MA/$FeSO_4$, respectively. During the pyrolysis, a significant volume expansion

DOI: 10.1021/acsnano.8b04693
ACS Nano 2018, 12, 9441–9450

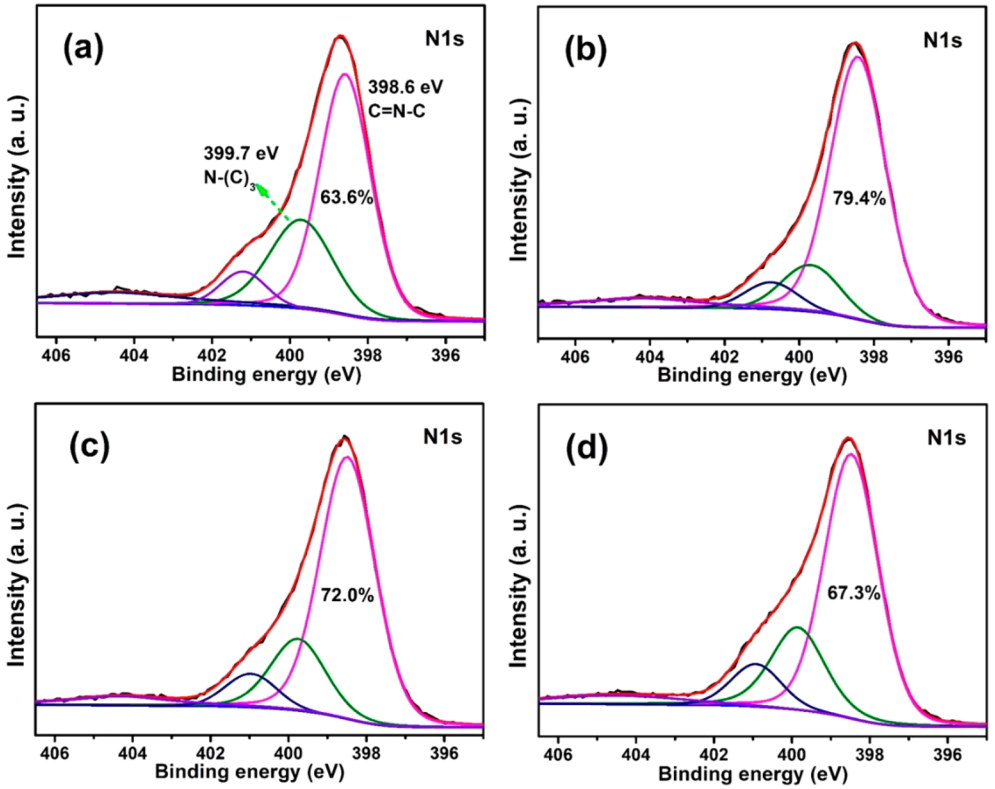

Figure 4. N 1s XPS spectra of (a) g-C_3N_4, (b) I-FeN_x/g-C_3N_4-5, (c) I-FeN_x/g-C_3N_4-10, and (d) I-FeN_x/g-C_3N_4-15.

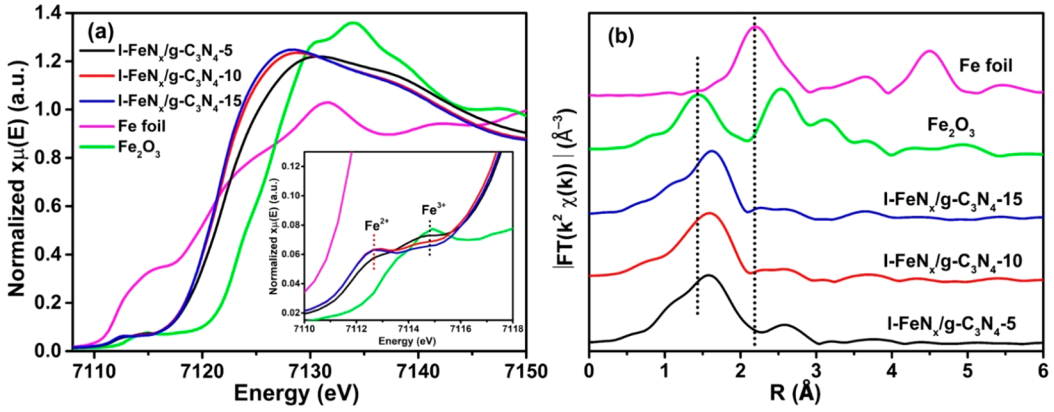

Figure 5. (a) K-edge XANES spectra and (b) R-space EXAFS magnitudes of different samples.

occurred accompanying the decomposition of Fe-ICC and MA, resulting in a brown foam-like solid as shown in Figure S1. While MIL-53 and $FeSO_4$ precursors were used, no obvious volume change occurred during pyrolysis. After the full decomposition of Fe-ICC and the repolymerization of MA to g-C_3N_4, highly dispersed Fe catalysts (I-FeN_x/g-C_3N_4-*X*) were obtained.

The XRD patterns of I-, M- and S-FeN_x/g-C_3N_4-*X* catalysts are shown in Figure S2. The primary diffraction peak (27.6°) in the patterns of catalysts is assigned to the (002) interlayer stacking from g-C_3N_4,[32] and this peak gradually becomes stronger as the MA-to-Fe precursor ratio *X* increases from 1 to 15. When *X* equals 1 and 2, diffraction peaks of Fe species were observed, and the peak intensity decreases as *X* increases from 5 to 15, suggesting that the Fe cluster size decreases with increasing *X*. Therefore, the amount of melamine (or the melamine to Fe-ICC ratio) has a crucial impact on the size distribution of the Fe species, *i.e.*, the Fe cluster size decreases as increasing the MA-to-Fe-ICC ratio. SEM images (FigureS3) also show that the layered structure of g-C_3N_4 increases in these catalysts as the MA-to-Fe-ICC ratio increases, and the I-FeN_x/g-C_3N_4-5 sample shows a fluffier structure. As shown in Figures 3a and S5, fragment-like structures of g-C_3N_4 were observed in the TEM images, but no iron nanoparticles were observed. The high-density Fe sites were confirmed by the sub-Angstrom resolution HAADF-STEM measurements. As shown in Figures 3b and S6a,b, a large number of ultra-small Fe clusters are uniformly dispersed in g-C_3N_4. Further examination (Figures 3c and S6c) revealed that ultra-small clusters and single-atom Fe sites coexist in g-C_3N_4 with high density, corresponding to ultrahigh iron loading (18.2 wt %) in I-FeN_x/g-C_3N_4-5. In addition, there were only single-atom Fe sites uniformly dispersed in thin area of g-C_3N_4, as illustrated in Figure 3d and Figure S6d. Energy dispersive X-ray spectros-

DOI: 10.1021/acsnano.8b04693
ACS Nano 2018, 12, 9441−9450

copy (EDS) images (Figures 3e and S7) show that C, N, and Fe elements are also uniformly distributed.

The N 1s XPS spectrum of g-C_3N_4 can be simulated using three peaks (Figure 4a). The peaks at binding energies of 398.6, 399.7, and 400.6 eV correspond to the sp^2 C=N−C bonds in the tri-s-triazine (pyridinic N), sp^3 tertiary nitrogen N−$(C)_3$ groups, and N−H groups, respectively.[33,34] Compared to g-C_3N_4, the spectra of I-FeN_x/g-C_3N_4-5, -10, and -15 (Figure 4a−c) can also be simulated with the three peaks, indicating that the structure of g-C_3N_4 remained in catalysts. It is worth noting that the content of pyridinic N increases in catalysts versus g-C_3N_4 (79.4%, 72.0%, 67.3%, and 63.6% for I-FeN_x/g-C_3N_4-5, -10, and -15 and g-C_3N_4, respectively), which is more favorable to binding with Fe atoms.[35,36] Meanwhile, the N 1s signal in these catalysts all shift toward the lower binding energy side in comparison to g-C_3N_4 because of the high content of Fe dopants in g-C_3N_4 matrix and the presence of Fe−N_x bonding. In the Fe 2p spectra (Figure S10), the peaks at 713.6 and 726.8 eV are assigned to Fe $2p_{3/2}$ and Fe $2p_{1/2}$ of Fe(III), respectively. The dominant peaks at 710.1 and 723.3 eV correspond to Fe $2p_{3/2}$ and Fe $2p_{1/2}$ of Fe(II), respectively.[37] The majority of Fe atoms are in the Fe(II) state for all I-FeN_x/g-C_3N_4-*X* catalysts (53.2%, 64.3%, 71.3%, and 72.0% of I-FeN_x/g- C_3N_4-2, -5, -10, and -15 catalysts, respectively). We can rule out the possible presence of FeC_x because the peaks of FeC_x are located at lower-binding-energy side, different from our catalysts.[38] As shown in Figure 5a, two small pre-edge peaks at 7112.6 and 7114.8 eV are present for all the catalysts in the Fe K-edge X-ray absorption near-edge structure (XANES) spectra, suggesting the presence of both Fe(II) and Fe(III) consistent with the XPS results as well as the ^{57}Fe Mössbauer spectra, as shown in Table S2. The small pre-edge peaks originate from the 1s−3d transition, indicating the localization of 3d orbitals in our catalysts, contrary to the delocalized 3d orbitals in iron carbides and nitrides. In addition, iron carbides have XANES energies similar to that of metallic Fe, which is not observed in these samples.[39]

The ^{57}Fe Mössbauer spectra of I-FeN_x/g-C_3N_4-5, M-FeN_x/g-C_3N_4-5, and S-FeN_x/g-C_3N_4-5 are shown in Figures 6a and S11, with analysis results given in Tables S2 and S3. All catalysts are fitted with three doublets (D1−D3).[35,40] The doublet D1, with smaller isomer shift (IS) values, is assigned to Fe(III), and the two quadrupole-splitting doublets (D2, D3) correspond to high-spin Fe(II) in different coordination sites.[41,42] The large quadrupole-splitting value for this high-spin Fe(II) indicates a complex coordination environment, as expected from Fe−N_x species.[43,44] The highest content (66%) of D2 and D3 sites in all iron species suggests that most of iron ions are converted into Fe(II)-N_x species in I-FeN_x/g-C_3N_4-5 catalyst (Tables S2 and S3).[45] The Bader charge of +1.097 and +1.094 are also consistent with a high content Fe(II) state in g-C_3N_4, as shown in Table S1.

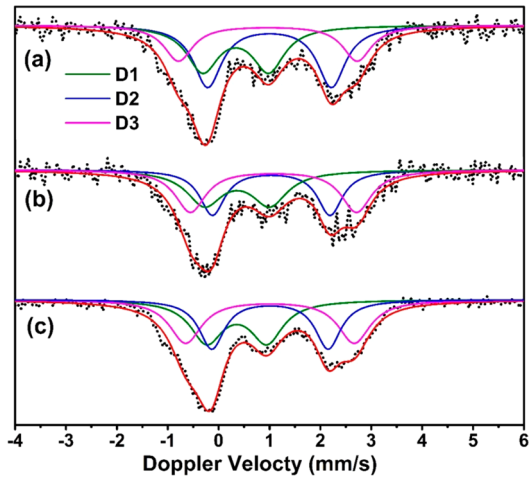

Figure 6. Room-temperature ^{57}Fe Mössbauer spectra of I-FeN_x/g-C_3N_4-5 catalyst: (a) fresh catalyst, (b) after the first cycle, and (c) after the second cycle.

Extended X-ray absorption fine structure (EXAFS) results of the catalysts are also consistent with the proposed Fe−N_x structure. As shown in Figure 5b, the first shell peaks at ∼1.6 Å (phase-uncorrected distance) of the catalysts suggest longer bond distances than the Fe−O bonds in Fe_2O_3 at ∼1.5 Å. The EXAFS fitting results indicate that the Fe−N bonds are at ∼2.09 Å, which is in the normal range of Fe−N bond distances (Table S4). The average coordination number of the catalysts are ∼4, suggesting the presence of coordinatively unsaturated Fe sites, which is desired for efficient catalysis. The absence of a large higher shell peak (within 2−3 Å) is consistent with the STEM results that all the Fe sites in the catalysts are highly dispersed ultra-small clusters and single atoms. The decrease of the second shell peak (at ∼2.6 Å) with increasing *X* suggests that the Fe species are dominantly single-atom sites, and the results are also consistent with the XRD results. We performed thermogravimetric analysis (TGA) to study the formation process of the catalysts using I-FeN_x/g-C_3N_4-5 as the example. The reaction to generate g-C_3N_4 is an integration of polyaddition and polycondensation accompanied by ammonia elimination. The TGA curves are given in Figure S12. At approximately 438 °C, the Fe-ICC begins to decompose, rapidly releasing iron species, and the decomposition of Fe-ICC is completed at 475 °C. This temperature range coincides with that for MA rearrangements (390−500 °C), during which the tri-*s*-triazine moiety is generated, and the iron species released by Fe-ICC decomposition can be captured by melamine/tri-s-triazine units due to the coordination between iron ions and N atoms. At 500 °C tri-*s*-triazine units start to polymerize,[46] accompanied by the incorporation of Fe clusters in the g-C_3N_4 matrices. After volume expansion, the resulting catalyst is fluffy, and well-dispersed ultra-small clusters and single-atom Fe sites are supported on g-C_3N_4. The iron loading of I-FeN_x/g-C_3N_4-5 was determined to be 18.2 wt % (Figure S13 and Table S5). For nanoclusters catalysts, increase of the metal loading often leads to the formation of large metal nanoparticles.[47] Fortunately, the abundant N anchoring sites in g-C_3N_4 and the *in situ* synthetic route allow for a high level of metal loading for nanocluster catalysts.

The degradation of methylene blue (MB) was selected as a probe reaction to evaluate the performance of FeN_x/g-C_3N_4 catalysts. All reactions were carried out at neutral pH. As shown in Figure 7a, I-FeN_x/g-C_3N_4-5 exhibits a high removal efficiency of MB in the photo-Fenton reaction, and the removal efficiency reached 60.0% within 2 min and 98.9% within 11 min, which is attributed to the high density of Fe(II)-N_x active sites (the period between 0 and 30 min represents adsorption−desorption equilibrium between catalyst and organics). We investigated the influence of H_2O_2 and visible light on the heterogeneous photo-Fenton process. From Figure S14, the I-FeN_x/g-C_3N_4-5 catalyst could effectively degrade high-concentration MB under H_2O_2 or H_2O_2 with

DOI: 10.1021/acsnano.8b04693
ACS Nano 2018, 12, 9441−9450

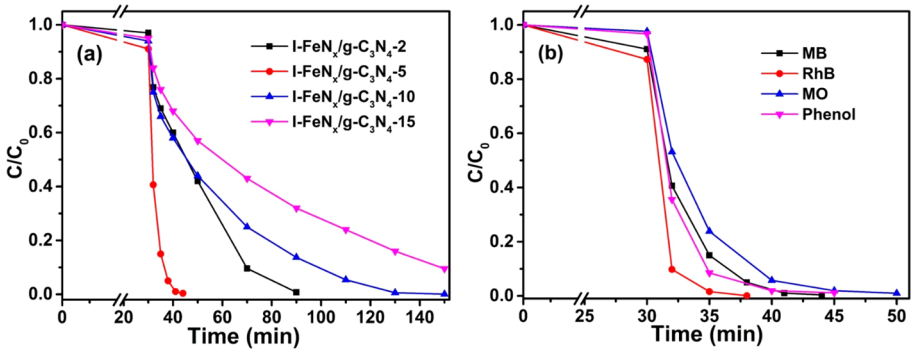

Figure 7. (a) Removal efficiency of MB using I-FeN$_x$/g-C$_3$N$_4$-X catalysts. (b) Removal efficiency of different organic pollutants using I-FeN$_x$/g-C$_3$N$_4$-5 catalyst. Reaction conditions: 200 mg L^{-1} organics (MB, MO, RhB, and phenol), 77 mM H_2O_2, 0.5 g L^{-1} catalyst, 308 K, and visible light.

Table 1. Comparison of the Catalytic Activities of I-FeN$_x$/g-C$_3$N$_4$-5 with the Fe-Based Catalysts in the Literature

catalysts	organics	m_{Cat} (g/L)	C_{Org} (ppm)	$C_{H_2O_2}$ (mM)	T (°C)	t (min)	conversion (%)	ref
Fe/MnO$_2$	MB	0.5	100	1647	25	120	94	48
10%Fe-g-C$_3$N$_4$	MB	0.5	50	200	25	90	100	49
FeOCl	MB	0.2	80	16	40	30	21	50
Fe-g-C$_3$N$_4$/GMC	RhB	0.8	50	40	25	40	95	51
Fe$_3$O$_4$/MIL-101	RhB	0.5	10	20	25	30	100	52
Fe$_2$O$_3$@hier-S-1	phenol	2	1000	149	50	60	100	53
FePc/graphene	phenol	0.2	50	49	25	180	77	54
Fe-ZSM-5	phenol	2	50	9	35	180	100	55
FeOCl	phenol	0.2	100	16	40	30	100	50
I-FeN$_x$/g-C$_3$N$_4$-5	MB	0.5	200	77	35	11	99	this work
	RhB					8	100	
	phenol					10	98	

visible light. We also compared the performance of I-FeN$_x$/g-C$_3$N$_4$ catalysts made with different precursor ratios (Figure 7a). The I-FeN$_x$/g-C$_3$N$_4$-5 catalyst exhibits the highest catalytic activity. During the pyrolysis, N-containing MA releases the reducing gas (ammonia) during its polycondensation to g-C$_3$N$_4$, which facilitates Fe(II)-N$_x$ species generation.[24,56] However, the excessive addition of MA will reduce the iron loading. The optimal ratio of MA over Fe-ICC is 5 for which both the iron loading and the amount of Fe(II)-N$_x$ active sites in catalyst can be maintained at a relatively high level. We next investigated the effect of varying Fe precursors on the activity of catalyst. The two nitrogen-free iron precursors generated M-FeN$_x$/g-C$_3$N$_4$ and S-FeN$_x$/g-C$_3$N$_4$. Their photo-Fenton properties are shown in Figure S15. The optimal ratio of MA over iron precursors was also 5 for the two series, however, the I-FeN$_x$/g-C$_3$N$_4$-X catalysts exhibit higher activity than M and S catalysts with the same precursor ratio. This indicates that the Fe-ICC is a preferable precursor to prepare nanocluster catalysts in the Fe/MA system.

The highest content of Fe(II)-N$_x$ active sites in I-FeN$_x$/g-C$_3$N$_4$-5 corresponds to optimal activity. However, S-FeN$_x$/g-C$_3$N$_4$-5 has higher content of Fe(II)-N$_x$ species than M-FeN$_x$/g-C$_3$N$_4$-5, whereas the catalytic activity is lower due to its lower dispersion (Figure S4e,f). We attribute the high-density Fe(II)-N$_x$ sites of I-FeN$_x$/g-C$_3$N$_4$-5 to the better compatibility of N-containing Fe-ICC with MA compared with FeSO$_4$ and MIL-53(Fe) precursors. A practical heterogeneous Fenton-type catalyst must efficiently and nonselectively degrade various organic pollutants. Therefore, the degradation of several typical organic pollutants including MB, methyl orange (MO), rhodamine B (RhB), and phenol by I-FeN$_x$/g-C$_3$N$_4$-5 was also evaluated (Figure 7b). The removal efficiency of all of these organics reached 100% within 15 min at neutral pH. Compared with other conventional iron-based Fenton-type catalysts as listed in Table 1, the I-FeN$_x$/g-C$_3$N$_4$-5 catalyst exhibits much higher catalytic activity for degrading high-concentration organic pollutants at neutral pH. The involved radicals species generated during the photo-Fenton process were confirmed *via* electron paramagnetic resonance (EPR)/5,5-dimethyl-1-pyrroline N-oxide (DMPO) experiments. As shown in Figure 8, the generation of HO·, a strong oxidizing species with an oxidation potential of 2.8 V versus NHE was observed within 1 min of reaction time. A 4-fold characteristic

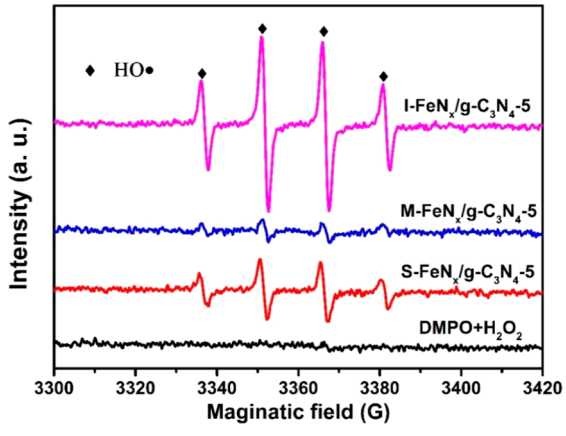

Figure 8. DMPO-trapped EPR spectra of three reaction systems and an H_2O_2−aqueous system at 1 min.

DOI: 10.1021/acsnano.8b04693
ACS Nano 2018, 12, 9441−9450

peak with an intensity ratio of 1:2:2:1 corresponds to the typical HO·/DMPO complex adduct.[10,57] The amount of HO· generated in the I-FeN$_x$/g-C$_3$N$_4$-5 catalytic system is much higher than the other two reaction systems, demonstrating that the high-density Fe(II)-N$_x$ active centers could rapidly activate H_2O_2 to generate HO·.

We have shown that the Fe species in I-FeN$_x$/g-C$_3$N$_4$-10 and 15 are dominantly single-atom sites, while in I-FeN$_x$/g-C$_3$N$_4$-5, ultra-small clusters and single-atom Fe sites coexist. To evaluate the role of various Fe species in Fenton reaction, we compared the MB removal rate (normalized by the weight of Fe in each catalyst) of catalysts with various clusters-to-single atom ratios. The clusters-to-single atom ratio decreases with increasing X, so if the Fe atoms in the ultra-small clusters show higher turnover rate than the single-atom Fe sites, a decrease of the turnover rate should be observed as increasing X, and *vice versa*. The calculated initial removal rate of MB for I-FeN$_x$/g-C$_3$N$_4$-5, 10, and 15 are 0.560, 0.528, and 0.478 g(MB)·min^{-1}·g(Fe)$^{-1}$, respectively (the rate was calculated using the data point at 2 min in Figure 7a). A slight decrease of the normalized turnover rate was observed as increasing X from 5 to 15, suggesting that single-atom Fe sites may have slightly lower turnover rates than the Fe atoms in ultra-small clusters. In summary, for catalysts with large single atom-to-cluster ratios, the single-atom Fe sites play a major role in Fenton reaction, while for catalysts with low single atom-to-cluster ratios, the Fe sites in ultra-small clusters play a major role. The g-C$_3$N$_4$ support stabilizes both highly active species, giving high dispersion at high metal loading, resulting in high activity.

The reusability of I-FeN$_x$/g-C$_3$N$_4$-5 is illustrated in Figure S16, and the removal efficiency of MB could reach almost 98% in 15 min for four cycles. The ^{57}Fe Mössbauer spectrum measurement was carried out to ascertain the iron state of the reused catalysts. After the first cycle, the total content of Fe(II) species is unchanged compared to the fresh catalyst, but there is a transformation between the two species (D2 and D3). Surprisingly, after further cycle experiment, the proportion of three iron species (D1−D3) is unchanged. It seems that the iron state of the reused catalyst tends to be stable after the first cycle. The result is consistent with the good reusability of I-FeN$_x$/g-C$_3$N$_4$-5 catalyst. The iron leaching for I, M, and S-FeN$_x$/g-C$_3$N$_4$-5 catalysts were 0.69, 0.79, and 2.44 mg/L, respectively, according to the inductively coupled plasma measurement (Table S7). The I-FeN$_x$/g-C$_3$N$_4$-5 catalyst has the minimal iron leaching that is much lower than the European Union standard of 2 mg/L, corresponding to the stable Fe(II)-N$_x$ configurations embedded in g-C$_3$N$_4$. The homogeneous catalysis of dissolved iron ions provides only a very small contribution to the total organics degradation in heterogeneous Fenton-like reaction at neutral pH (Figure S17).[58]

CONCLUSIONS

High-density ultra-small clusters and single-atom Fe sites were anchored in g-C$_3$N$_4$ matrices *via* a one-step pyrolysis of a Fe−N-containing precursor (Fe-ICC) with MA. The presence of abundant anchoring sites in g-C$_3$N$_4$ leads to highly dispersed Fe−N$_x$ sites, as illustrated using HAADF-STEM, XAS, XPS, and DFT calculations. Compared with other nitrogen-free iron precursors (FeSO$_4$ and Fe-MOF), Fe-ICC, together with MA, is a highly compatible precursor for the pyrolysis, which was crucial for generating high-density Fe−N$_x$ centers. In AOPs, the Fe(II)-N$_x$ active sites can rapidly activate H_2O_2 to generate HO· radicals, exhibiting excellent removal efficiency for various typical organics (MB, MO, RhB, and phenol), better reusability, and low iron leaching (0.69 mg/L). I-FeN$_x$/g-C$_3$N$_4$-5 may serve as a practical catalyst for organic pollutant degradation in wastewater. These findings demonstrate a potentially generalizable path toward the design and synthesis of nanocluster catalyst with a high density of active sites.

EXPERIMENTAL SECTION

All chemicals are analytical grade and used without further purification. Iron dichloride tetrahydrate ($FeCl_2·4H_2O$), ferrous sulfate heptahydrate ($FeSO_4·7H_2O$), methyl orange (MO), rhodamine B (RhB), phenol, and methylene blue (MB) were purchased from Damao Chemical Reagent Factory (Tianjin, China). *N*,*N*-Dimethylformamide (DMF), absolute methanol, 30% hydrogen peroxide aqueous solution (H_2O_2, 30%), and hydrofluoric acid (HF) were obtained from Guangfu Fine Chemical Research Institute (Tianjin, China). Polyvinylpyrrolidone (PVP), melamine (MA), terephthalic acid (BDC), 2-methylimidazole, and 5,5-dimethyl-1-pyrroline N-oxide (DMPO) were received from Aladdin (Shanghai, China).

Preparation of FeN$_x$/g-C$_3$N$_4$. *Synthesis of Fe-ICC.* Fe-ICC was synthesized by a ball milling method according to the reported synthesis route of ZIF-8 with modifications.[59] First, ferrous sulfate ($FeSO_4·7H_2O$, 3.335 g), 2-methylimidazole (4.72 g), PVP (4.32 g), and methanol solution (12 mL) were added into an agate jar, and then ball-milling was carried out at 500 rpm for 2 h. The resulting dark-green solid was centrifuged, washed with ethanol several times, and then dried at 60 °C overnight in a vacuum oven.

Synthesis of MIL-53 (Fe). The one-step synthesis of MIL-53 (Fe) was carried out under mild hydrothermal conditions according to the literature.[60] The reaction was performed in a 100 mL Teflon-lined stainless steel autoclave for 3 days at 220 °C. The amount of the starting reagents was 4 mmol $FeCl_2$ (0.8 g), 4 mmol BDC (0.67 g), 0.8 mL of HF (10% aqueous solution), and 40 mL of DMF. The product was obtained as a light yellow powder. Finally, the solid was washed with DMF and deionized water and then dried at 80 °C overnight.

Synthesis of FeN$_x$/g-C$_3$N$_4$. First, iron precursors and MA were fully ground in an agate mortar with varied ratios (MA/iron precursors ratios of 1, 2, 5, 10, and 15), and then the mixture was calcined at 600 °C for 5 h in a tube furnace with a ramping rate of 5 °C min^{-1} in nitrogen atmosphere. Before calcination, the mixture was placed into a quartz boat and the tube furnace was prepurged with nitrogen for 2 h. The resulting russet catalysts were named as I-FeN$_x$/g-C$_3$N$_4$-*X* (*X* = 1, 2, 5, 10, and 15). The other two series of composite catalysts were synthesized using the same procedure with different iron precursors, and the two series of as-synthesized catalysts were named as M-FeN$_x$/g-C$_3$N$_4$-X (MIL-53(Fe) as precursor, with *X* = 2, 5, and 10) and S-FeN$_x$/g-C$_3$N$_4$ ($FeSO_4$ as precursor, with *X* = 2, 5, and 10).

Physicochemical Characterization. Powder X-ray diffraction (XRD) patterns were recorded on a Rigaku Smartlab diffractometer with a nickel-filtered Cu Kα X-ray source at a scanning rate of 0.02° over the range between 5° and 80°. The tube voltage and current used were 45 kV and 200 mA, respectively. X-ray photoelectron spectroscopy (XPS) measurements were performed on a Thermo Scientific ESCA Lab250 spectrometer with a monochromatic Al Kα X-ray source. Binding energies were calibrated by the C 1s peak at 284.6 eV. High-angle annular dark field-scanning transmission electron microscopy (HAADF-STEM) and energy dispersive X-ray spectroscopy (EDS) images were collected using a probe-corrected JEM-ARM200F electron microscope operated at 200 kV. Transmission electron microscopy (TEM) images were taken on a Tecnai G2 20 S-twin instrument (FEI Company) with an acceleration voltage of 200 kV. The samples for TEM analysis were prepared by dipping the carbon-coated copper grids into ethanol solutions of the samples and drying at ambient conditions. TGA of the samples were performed on a SDT Q600 thermal gravimetric analyzer (TA

DOI: 10.1021/acsnano.8b04693
ACS Nano 2018, 12, 9441−9450

Instruments) from room temperature to 800 °C at a ramping rate of 10 °C min^{-1} under air or N_2 atmosphere. The dissolved iron concentration was detected by an inductively coupled plasma-atomic emission spectrometer (Optima 2000DV, USA). ^{57}Fe Mössbauer spectra were recorded at room temperature using a Topologic 500A spectrometer with a proportional counter. The involved radical species were confirmed using a Bruker electron paramagnetic resonance device (A200-9.5/12, Ger). XANES and EXAFS measurements at the Fe K-edge (7112 eV) were conducted on the bending magnet beamline of the Materials Research Collaborative Access Team (MRCAT, 10-BM) and Sector 20 at the advanced photon source (APS) at the Argonne National Laboratory. Ionization chambers were optimized at the midpoint of the Fe spectrum for the maximum current with linear response (~10^{10} photons detected per second) using 35% He in N_2 (15% absorption) in the incident X-ray detector and a mixture of ~17% Ar in N_2 (70% absorption) in the transmission X-ray detector. A third detector in the series simultaneously collected a Fe foil reference spectrum with each measurement for energy calibration. A cryogenically cooled double-crystal Si(111) monochromator was used and detuned to 50% to minimize the presence of harmonics. The X-ray beam was 0.5 mm × 1.5 mm, and data were collected in transmission geometry in 10 min in step-scan mode in air. All the samples were diluted and ground with BN and pressed into a pellet to get approximately an edge jump of 1.0. The data analysis was done using Demeter 0.9.26 software package.

Heterogeneous Photo-Fenton Degradation of Dyes and Phenol. Photo-Fenton catalytic activities of the catalysts were evaluated for degradation of four model organic pollutants (MB, MO, RhB, and phenol) with the addition of H_2O_2 under visible light irradiation at neutral pH. In a typical process, 25 mg of catalyst was added into 50 mL of organic solution (200 mg/L). The mixture was ultrasonicated for 10 min and then stirred for 30 min in the dark to establish adsorption−desorption equilibrium. The reaction was initiated by adding 400 μL of H_2O_2 (30 wt %) aqueous solution and simultaneously turning on a 300 W Xe arc lamp (PLS-SXE 300CUV, Beijing Perfect Light Co., Ltd.) with a UV-CUT filter to cut off light of wavelength of <420 nm. The temperature was kept at 308 K using recycled water. During illumination, approximately 400 μL of suspension was withdrawn at certain intervals after separation of catalyst using a filter and was analyzed by a UV−vis spectrophotometer (JASCO V570, Japan) or an Agilent high-performance liquid chromatograph (HPLC 1200) with an Eclipse XDB-C18 (150 mm × 4.6 mm × 5 μm) column. The photocatalytic activities of catalysts were calculated by the concentration of dye (C/C_0) according to the absorbance (A/A_0), where C_0 and A_0 were the initial concentration and absorbance of dye, respectively.

In recycling experiment, the catalyst was repeatedly applied to remove MB by photo-Fenton reaction. After each cycle, catalyst was centrifugally separated and then dried at 80 °C overnight. The same amount of dried sample was used as a catalyst for the next recycling experiment.

Computational Methods. Theoretical calculations were performed using the Vienna *ab initio* simulation package. (VASP).[61] The generalized gradient approximation (GGA) in the form of the Perdew−Burke−Ernzerhof (PBE) functional was adopted for the exchange-correlation interactions.[62] The cutoff energy for the plane-wave basis set was set to 500 eV. The optimized lattice parameters for pure g-C_3N_4 ($a = b = 6.96$ Å and $c = 7.51$ Å) are in good agreement with other theoretical results ($a = b = 6.97$ Å and $c = 7.14$ Å). The two-layer g-C_3N_4 (001) slabs were built with 2 × 2 supercells with a vacuum region of 15 Å between slabs. A set of 3 × 3 × 1 Monkhorst−Pack special k-points has been used for structural relaxations to search for the most stable configurations. The convergence criteria for the residual force on each atom during structure relaxation were set to 0.01 eV/Å. A refined 5 × 5 × 1 Monkhorst−Pack special k-point mesh is used for the most stable surface configurations to obtain more accurate energies.

We calculated the Fe binding energy at various adsorption sites in g-C_3N_4 including the 6-fold cavity, the top of a 6-membered ring, and between the 2 layers. The single Fe atom binding energy is defined as eq 1:

$$E_{\text{binding}=}(E_{\text{Fe/g-C}_3\text{N}_4} - E_{\text{g-C}_3\text{N}_4} - nE_{\text{Fe}})/n \quad (1)$$

where $E_{\text{Fe/g-C}_3\text{N}_4}$, E_{Fe}, and $E_{\text{g-C}_3\text{N}_4}$ are the total energies of single Fe atom adsorbed on g-C_3N_4, an isolated Fe atom, and the bare g-C_3N_4, respectively. Here, n is the number of Fe atoms. For the binding of Fe_2 clusters, the binding energy is also referenced to an isolated Fe atom and expressed on a per-Fe-atom basis. A more-negative binding energy indicates stronger interaction between Fe atoms and g-C_3N_4.

ASSOCIATED CONTENT

Supporting Information

The Supporting Information is available free of charge on the ACS Publications website at DOI: 10.1021/acsnano.8b04693.

Tables showing calculated Fe binding energy, Bader charge, and Fe−N distance; Mössbauer parameters; EXAFS fitting results; iron loadings; element contents of samples; and ICP results. Figures showing the overall appearance of precursors and catalyst; XRD patterns; SEM, HRTEM, and HAADF-STEM images; MB removal efficiency; reusability; XPS and Mössbauer spectra; and TG curves (PDF)

AUTHOR INFORMATION

Corresponding Authors

*E-mail: keyanli@dlut.edu.cn.
*E-mail: guoxw@dlut.edu.cn.

ORCID

Guanghui Zhang: 0000-0002-5854-6909
Chunshan Song: 0000-0003-2344-9911
Junhu Wang: 0000-0003-1987-2522
Xinwen Guo: 0000-0002-6597-4979

Author Contributions

#S. A. and G. Z. contributed equally to this work.

Notes

The authors declare no competing financial interest.

ACKNOWLEDGMENTS

This work was supported by the National Natural Science Foundation of China (grant nos. 21401017 and 21236008), the Fundamental Research Funds for the Central Universities (grant no. DUT16LK12) and the Qianren Program of China at DUT. G.Z. and J.T.M. were supported in part by the National Science Foundation under cooperative agreement no. EEC-1647722. Use of the Advanced Photon Source is supported by the U.S. Department of Energy, Office of Science, and Office of Basic Energy Sciences under contract no. DE-AC02-06CH11357. Materials Research Collaborative Access Team (MRCAT, Sector 10-BM) operations are supported by the Department of Energy and the MRCAT member institutions. Sector 20 operations are supported by the US Department of Energy and the Canadian Light Source.

REFERENCES

(1) Wang, C.-C.; Li, J.-R.; Lv, X.-L.; Zhang, Y.-Q.; Guo, G. Photocatalytic Organic Pollutants Degradation in Metal-Organic Frameworks. *Energy Environ. Sci.* **2014**, *7*, 2831−2867.

(2) Tušar, N. N.; Maučec, D.; Rangus, M.; Arčon, I.; Mazaj, M.; Cotman, M.; Pintar, A.; Kaučič, V. Manganese Functionalized Silicate Nanoparticles as a Fenton-Type Catalyst for Water Purification by

DOI: 10.1021/acsnano.8b04693
ACS Nano 2018, 12, 9441−9450

Advanced Oxidation Processes (AOP). *Adv. Funct. Mater.* **2012**, *22*, 820−826.
(3) Hao, S. M.; Qu, J.; Zhu, Z. S.; Zhang, X. Y.; Wang, Q. Q.; Yu, Z. Z. Hollow Manganese Silicate Nanotubes with Tunable Secondary Nanostructures as Excellent Fenton-Type Catalysts for Dye Decomposition at Ambient Temperature. *Adv. Funct. Mater.* **2016**, *26*, 7334−7342.
(4) Zhang, R.; Liu, Y.; He, M.; Su, Y.; Zhao, X.; Elimelech, M.; Jiang, Z. Antifouling Membranes for Sustainable Water Purification: Strategies and Mechanisms. *Chem. Soc. Rev.* **2016**, *45*, 5888−5924.
(5) Ong, W.-J.; Tan, L.-L.; Ng, Y. H.; Yong, S.-T.; Chai, S.-P. Graphitic Carbon Nitride ($g\text{-}C_3N_4$)-Based Photocatalysts for Artificial Photosynthesis and Environmental Remediation: Are We a Step Closer to Achieving Sustainability? *Chem. Rev.* **2016**, *116*, 7159−7329.
(6) Fujihira, M.; Satoh, Y.; Osa, T. Heterogeneous Photocatalytic Oxidation of Aromatic Compounds on TiO_2. *Nature* **1981**, *293*, 206−208.
(7) Tzirakis, M. D.; Lykakis, I. N.; Orfanopoulos, M. Decatungstate as an Efficient Photocatalyst in Organic Chemistry. *Chem. Soc. Rev.* **2009**, *38*, 2609−2621.
(8) Dramou, B. J.; Shah, V.; Pinto, J. M. A Kinetic Model for Microbial Decontamination of Water Based on a Modified Fenton Reaction. *Energy Environ. Sci.* **2008**, *1*, 395−402.
(9) Xing, M.; Xu, W.; Dong, C.; Bai, Y.; Zeng, J.; Zhou, Y.; Zhang, J.; Yin, Y. Metal Sulfides as Excellent Co-Catalysts for H_2O_2 Decomposition in Advanced Oxidation Processes. *Chem.* **2018**, 1−14.
(10) Li, X.; Ao, Z.; Liu, J.; Sun, H.; Rykov, A. I.; Wang, J. Topotactic Transformation of Metal-Organic Frameworks to Graphene-Encapsulated Transition-Metal Nitrides as Efficient Fenton-Like Catalysts. *ACS Nano* **2016**, *10*, 11532−11540.
(11) Martínez, F.; Calleja, G.; Melero, J. A.; Molina, R. Iron Species Incorporated over Different Silica Supports for the Heterogeneous Photo-Fenton Oxidation of Phenol. *Appl. Catal., B* **2007**, *70*, 452−460.
(12) Guzman, J.; Gates, B. C. Supported Molecular Catalysts: Metal Complexes and Clusters on Oxides and Zeolites. *Dalton Trans* **2003**, *17*, 3303−3318.
(13) He, L.; Weniger, F.; Neumann, H.; Beller, M. Synthesis, Characterization, and Application of Metal Nanoparticles Supported on Nitrogen-Doped Carbon: Catalysis Beyond Electrochemistry. *Angew. Chem., Int. Ed.* **2016**, *55*, 12582−12594.
(14) Georgakilas, V.; Tiwari, J. N.; Kemp, K. C.; Perman, J. A.; Bourlinos, A. B.; Kim, K. S.; Zboril, R. Noncovalent Functionalization of Graphene and Graphene Oxide for Energy Materials, Biosensing, Catalytic, and Biomedical Applications. *Chem. Rev.* **2016**, *116*, 5464−5519.
(15) Kasiri, M. B.; Aleboyeh, H.; Aleboyeh, A. Degradation of Acid Blue 74 Using Fe-ZSM5 Zeolite as a Heterogeneous Photo-Fenton Catalyst. *Appl. Catal., B* **2008**, *84*, 9−15.
(16) Xu, L.; Wang, J. Magnetic Nanoscaled Fe_3O_4/CeO_2 Composite as an Efficient Fenton-Like Heterogeneous Catalyst for Degradation of 4-Chlorophenol. *Environ. Sci. Technol.* **2012**, *46*, 10145−10153.
(17) Li, X.; Yu, J.; Wageh, S.; Al-Ghamdi, A. A.; Xie, J. Graphene in Photocatalysis: A Review. *Small* **2016**, *12*, 6640−6696.
(18) Buchwalter, P.; Rose, J.; Braunstein, P. Multimetallic Catalysis Based on Heterometallic Complexes and Clusters. *Chem. Rev.* **2015**, *115*, 28−126.
(19) Li, H.; Wang, S.; Sawada, H.; Han, G. G. D.; Samuels, T.; Allen, C. S.; Kirkland, A. I.; Grossman, J. C.; Warner, J. H. Atomic Structure and Dynamics of Single Platinum Atom Interactions with Monolayer MoS_2. *ACS Nano* **2017**, *11*, 3392−3403.
(20) Sun, Q.; Wang, N.; Bing, Q.; Si, R.; Liu, J.; Bai, R.; Zhang, P.; Jia, M.; Yu, J. Subnanometric Hybrid Pd-$M(OH)_2$, M = Ni, Co, Clusters in Zeolites as Highly Efficient Nanocatalysts for Hydrogen Generation. *Chem.* **2017**, *3*, 477−493.
(21) Yang, X.; Sun, J.-K.; Kitta, M.; Pang, H.; Xu, Q. Encapsulating Highly Catalytically Active Metal Nanoclusters Inside Porous Organic Cages. *Nat. Catal.* **2018**, *1*, 214−220.
(22) Liu, W.; Zhang, L.; Yan, W.; Liu, X.; Yang, X.; Miao, S.; Wang, W.; Wang, A.; Zhang, T. Single-Atom Dispersed Co-N-C Catalyst: Structure Identification and Performance for Hydrogenative Coupling of Nitroarenes. *Chem. Sci.* **2016**, *7*, 5758−5764.
(23) Fei, H.; Dong, J.; Feng, Y.; Allen, C. S.; Wan, C.; Volosskiy, B.; Li, M.; Zhao, Z.; Wang, Y.; Sun, H.; An, P.; Chen, W.; Guo, Z.; Lee, C.; Chen, D.; Shakir, I.; Liu, M.; Hu, T.; Li, Y.; Kirkland, A. I.; Duan, X.; Huang, Y. General Synthesis and Definitive Structural Identification of MN_4C_4 Single-Atom Catalysts with Tunable Electrocatalytic Activities. *Nat. Catal.* **2018**, *1*, 63−72.
(24) Wu, H.; Li, H.; Zhao, X.; Liu, Q.; Wang, J.; Xiao, J.; Xie, S.; Si, R.; Yang, F.; Miao, S.; Guo, X.; Wang, G.; Bao, X. Highly Doped and Exposed Cu(I)-N Active Sites within Graphene towards Efficient Oxygen Reduction for Zinc-Air Batteries. *Energy Environ. Sci.* **2016**, *9*, 3736−3745.
(25) Yin, P.; Yao, T.; Wu, Y.; Zheng, L.; Lin, Y.; Liu, W.; Ju, H.; Zhu, J.; Hong, X.; Deng, Z.; Zhou, G.; Wei, S.; Li, Y. Single Cobalt Atoms with Precise N-Coordination as Superior Oxygen Reduction Reaction Catalysts. *Angew. Chem., Int. Ed.* **2016**, *55*, 10800−10805.
(26) Zhang, L.; Jia, Y.; Gao, G.; Yan, X.; Chen, N.; Chen, J.; Soo, M. T.; Wood, B.; Yang, D.; Du, A.; Yao, X. Graphene Defects Trap Atomic Ni Species for Hydrogen and Oxygen Evolution Reactions. *Chem.* **2018**, *4*, 285−297.
(27) Li, X.; Bi, W.; Zhang, L.; Tao, S.; Chu, W.; Zhang, Q.; Luo, Y.; Wu, C.; Xie, Y. Single-Atom Pt as Co-Catalyst for Enhanced Photocatalytic H_2 Evolution. *Adv. Mater.* **2016**, *28*, 2427−2431.
(28) Cheng, N.; Stambula, S.; Wang, D.; Banis, M. N.; Liu, J.; Riese, A.; Xiao, B.; Li, R.; Sham, T. K.; Liu, L. M.; Botton, G. A.; Sun, X. Platinum Single-Atom and Cluster Catalysis of the Hydrogen Evolution Reaction. *Nat. Commun.* **2016**, *7*, 13638.
(29) Chen, Z.; Pronkin, S.; Fellinger, T.-P.; Kailasam, K.; Vilé, G.; Albani, D.; Krumeich, F.; Leary, R.; Barnard, J.; Thomas, J. M.; Pérez-Ramírez, J.; Antonietti, M.; Dontsova, D. Merging Single-Atom-Dispersed Silver and Carbon Nitride to a Joint Electronic System *via* Copolymerization with Silver Tricyanomethanide. *ACS Nano* **2016**, *10*, 3166−3175.
(30) Vile, G.; Albani, D.; Nachtegaal, M.; Chen, Z.; Dontsova, D.; Antonietti, M.; Lopez, N.; Perez-Ramirez, J. A Stable Single-Site Palladium Catalyst for Hydrogenations. *Angew. Chem., Int. Ed.* **2015**, *54*, 11265−11269.
(31) Gao, G.; Jiao, Y.; Waclawik, E. R.; Du, A. Single Atom (Pd/Pt) Supported on Graphitic Carbon Nitride as an Efficient Photocatalyst for Visible-Light Reduction of Carbon Dioxide. *J. Am. Chem. Soc.* **2016**, *138*, 6292−6297.
(32) Wang, X.; Maeda, K.; Thomas, A.; Takanabe, K.; Xin, G.; Carlsson, J. M.; Domen, K.; Antonietti, M. A Metal-Free Polymeric Photocatalyst for Hydrogen Production from Water Under Visible Light. *Nat. Mater.* **2009**, *8*, 76−80.
(33) Jiang, Z.; Wan, W.; Li, H.; Yuan, S.; Zhao, H.; Wong, P. K. A Hierarchical Z-Scheme Alpha-$Fe_2O_3/g\text{-}C_3N_4$ Hybrid for Enhanced Photocatalytic CO_2 Reduction. *Adv. Mater.* **2018**, *30*, 1706108.
(34) Cui, X.; Yang, S.; Yan, X.; Leng, J.; Shuang, S.; Ajayan, P. M.; Zhang, Z. Pyridinic-Nitrogen-Dominated Graphene Aerogels with Fe-N-C Coordination for Highly Efficient Oxygen Reduction Reaction. *Adv. Funct. Mater.* **2016**, *26*, 5708−5717.
(35) Li, J.; Ghoshal, S.; Liang, W.; Sougrati, M.-T.; Jaouen, F.; Halevi, B.; McKinney, S.; McCool, G.; Ma, C.; Yuan, X.; Ma, Z.-F.; Mukerjee, S.; Jia, Q. Structural and Mechanistic Basis for the High Activity of Fe-N-C Catalysts toward Oxygen Reduction. *Energy Environ. Sci.* **2016**, *9*, 2418−2432.
(36) Artyushkova, K.; Serov, A.; Rojas-Carbonell, S.; Atanassov, P. Chemistry of Multitudinous Active Sites for Oxygen Reduction Reaction in Transition Metal-Nitrogen-Carbon Electrocatalysts. *J. Phys. Chem. C* **2015**, *119*, 25917−25928.
(37) Li, J.-S.; Li, S.-L.; Tang, Y.-J.; Han, M.; Dai, Z.-H.; Bao, J.-C.; Lan, Y.-Q. Nitrogen-doped Fe/Fe_3C@Graphitic Layer/Carbon Nanotube Hybrids Derived From MOFs: Efficient Bifunctional Electrocatalysts for ORR and OER. *Chem. Commun.* **2015**, *51*, 2710−2713.

DOI: 10.1021/acsnano.8b04693
ACS Nano 2018, 12, 9441−9450

(38) Park, J. C.; Yeo, S. C.; Chun, D. H.; Lim, J. T.; Yang, J.-I.; Lee, H.-T.; Hong, S.; Lee, H. M.; Kim, C. S.; Jung, H. Highly Activated K-doped Iron Carbide Nanocatalysts Designed by Computational Simulation for Fischer−Tropsch Synthesis. *J. Mater. Chem. A* **2014**, *2*, 14371−14379.
(39) Zhao, H.; Zhu, Q.; Gao, Y.; Zhai, P.; Ma, D. Iron Oxide Nanoparticles Supported on Pyrolytic Graphene Oxide as Model Catalysts for Fischer−Tropsch Synthesis. *Appl. Catal., A* **2013**, *456*, 233−239.
(40) Koslowski, U. I.; Abs-Wurmbach, I.; Fiechter, S.; Bogdanoff, P. Nature of the Catalytic Centers of Porphyrin-Based Electrocatalysts for the ORR: A Correlation of Kinetic Current Density with the Site Density of Fe-N_4 Centers. *J. Phys. Chem. C* **2008**, *112*, 15356−15366.
(41) Zitolo, A.; Goellner, V.; Armel, V.; Sougrati, M. T.; Mineva, T.; Stievano, L.; Fonda, E.; Jaouen, F. Identification of Catalytic Sites for Oxygen Reduction in Iron- and Nitrogen-Doped Graphene Materials. *Nat. Mater.* **2015**, *14*, 937−942.
(42) Li, X.; Liu, J.; Rykov, A. I.; Han, H.; Jin, C.; Liu, X.; Wang, J. Excellent Photo-Fenton Catalysts of Fe-Co Prussian Blue Analogues and Their Reaction Mechanism Study. *Appl. Catal., B* **2015**, *179*, 196−205.
(43) Nazir, R.; Mazhar, M.; Siddique, M.; Hussain, S. T. Effect of Particle Size and Alloying with Different Metals on ^{57}Fe Mössbauer Spectra. In *ISIAME 2008: Proceedings of the International Symposium on the Industrial Applications of the Mössbauer Effect (ISIAME 2008) held in Budapest, Hungary, 17−22 August 2008*, Kuzmann, E.; Lázár, K., Eds.; Springer Berlin Heidelberg: Berlin, Germany, 2009; pp 85−95.
(44) Almeida, A. F. L.; Vasconcelos, I. F.; Valente, M. A.; Sombra, A. S. B. The Optical and ^{57}Fe Mössbauer Spectra of Lithium Diborate ($Li_2B_4O_7$) in Borophosphate Glass-Ceramics. *Phys. B* **2002**, *322*, 276−288.
(45) Li, X.; Wang, Z.; Zhang, B.; Rykov, A. I.; Ahmed, M. A.; Wang, J. $Fe_xCo_{3-x}O_4$ Nanocages Derived from Nanoscale Metal-Organic Frameworks for Removal of Bisphenol A by Activation of Peroxymonosulfate. *Appl. Catal., B* **2016**, *181*, 788−799.
(46) Zheng, Y.; Lin, L.; Wang, B.; Wang, X. Graphitic Carbon Nitride Polymers Toward Sustainable Photoredox Catalysis. *Angew. Chem., Int. Ed.* **2015**, *54*, 12868−12884.
(47) Wu, G.; More, K. L.; Johnston, C. M.; Zelenay, P. High-Performance Electrocatalysts for Oxygen Reduction Derived from Polyaniline, Iron, and Cobalt. *Science* **2011**, *332*, 443−447.
(48) Huang, R.; Liu, Y.; Chen, Z.; Pan, D.; Li, Z.; Wu, M.; Shek, C.-H.; Wu, C. M. L.; Lai, J. K. L. Fe-Species-Loaded Mesoporous MnO_2 Superstructural Requirements for Enhanced Catalysis. *ACS Appl. Mater. Interfaces* **2015**, *7*, 3949−3959.
(49) Bicalho, H. A.; Lopez, J. L.; Binatti, I.; Batista, P. F. R.; Ardisson, J. D.; Resende, R. R.; Lorençon, E. Facile Synthesis of Highly Dispersed Fe(II)-Doped g-C_3N_4 and Its Application in Fenton-Like Catalysis. *Molecular Catalysis* **2017**, *435*, 156−165.
(50) Yang, X. J.; Xu, X. M.; Xu, J.; Han, Y. F. Iron Oxychloride (FeOCl): An Efficient Fenton-Like Catalyst for Producing Hydroxyl Radicals in Degradation of Organic Contaminants. *J. Am. Chem. Soc.* **2013**, *135*, 16058−16061.
(51) Ma, J.; Yang, Q.; Wen, Y.; Liu, W. Fe-g-C_3N_4/Graphitized Mesoporous Carbon Composite as an Effective Fenton-Like Catalyst in a Wide pH Range. *Appl. Catal., B* **2017**, *201*, 232−240.
(52) Zhao, C.; Dong, P.; Liu, Z.; Wu, G.; Wang, S.; Wang, Y.; Liu, F. Facile Synthesis of Fe_3O_4/MIL-101 Nanocomposite as an Efficient Heterogeneous Catalyst for Degradation of Pollutants in Fenton-Like System. *RSC Adv.* **2017**, *7*, 24453−24461.
(53) Dai, C.; Zhang, A.; Liu, M.; Gu, L.; Guo, X.; Song, C. Hollow Alveolus-Like Nanovesicle Assembly with Metal-Encapsulated Hollow Zeolite Nanocrystals. *ACS Nano* **2016**, *10*, 7401−7408.
(54) Wang, Q.; Li, H.; Yang, J.-H.; Sun, Q.; Li, Q.; Yang, J. Iron Phthalocyanine-Graphene Donor-Acceptor Hybrids for Visible-Light-Assisted Degradation of Phenol in the Presence of H_2O_2. *Appl. Catal., B* **2016**, *192*, 182−192.
(55) Gonzalez-Olmos, R.; Martin, M. J.; Georgi, A.; Kopinke, F.-D.; Oller, I.; Malato, S. Fe-Zeolites as Heterogeneous Catalysts in Solar Fenton-Like Reactions at Neutral pH. *Appl. Catal., B* **2012**, *125*, 51−58.
(56) Zhang, S.; Zhang, H.; Liu, Q.; Chen, S. Fe-N Doped Carbon Nanotube/Graphene Composite: Facile Synthesis and Superior Electrocatalytic Activity. *J. Mater. Chem. A* **2013**, *1*, 3302−3308.
(57) Yamazaki, I.; Piette, L. H. EPR Spin-trapping Study on the Oxidizing Species Formed in the Reaction of the Ferrous Ion with Hydrogen Peroxide. *J. Am. Chem. Soc.* **1991**, *113*, 7588−7593.
(58) Wang, M.; Fang, G.; Liu, P.; Zhou, D.; Ma, C.; Zhang, D.; Zhan, J. Fe_3O_4@β-CD Nanocomposite as Heterogeneous Fenton-Like Catalyst for Enhanced Degradation of 4-Chlorophenol (4-CP). *Appl. Catal., B* **2016**, *188*, 113−122.
(59) Bennett, T. D.; Cao, S.; Tan, J. C.; Keen, D. A.; Bithell, E. G.; Beldon, P. J.; Friscic, T.; Cheetham, A. K. Facile Mechanosynthesis of Amorphous Zeolitic Imidazolate Frameworks. *J. Am. Chem. Soc.* **2011**, *133*, 14546−14549.
(60) Sun, Q.; Liu, M.; Li, K.; Han, Y.; Zuo, Y.; Wang, J.; Song, C.; Zhang, G.; Guo, X. Controlled Synthesis of Mixed-Valent Fe-Containing Metal Organic Frameworks for the Degradation of Phenol Under Mild Conditions. *Dalton Trans* **2016**, *45*, 7952−7959.
(61) Kresse, G.; Furthmüller, J. Efficient Iterative Schemes for *ab initio* Total-Energy Calculations Using a Plane-Wave Basis Set. *Phys. Rev. B: Condens. Matter Mater. Phys.* **1996**, *54*, 11169−11186.
(62) Perdew, J. P.; Burke, K.; Ernzerhof, M. Generalized Gradient Approximation Made Simple. *Phys. Rev. Lett.* **1996**, *77*, 3865−3868.

DOI: 10.1021/acsnano.8b04693
ACS Nano 2018, 12, 9441−9450